International Journal of High Speed Electronics and Systems, Vol. 12, No. 4 (2002) 995–1024

Generation of Terahertz Emission Based on Intersubband Transitions

Qing Hu
Department of Electrical Engineering and Computer Science and Research Laboratory of Electronics, Massachusetts Institute of Technology, Cambridge, MA 02139, USA

In this chapter, we present our work on the development of coherent THz sources based on intersubband transition in quantum-well structures. The main focus is on electrically pumped or quantum-cascade structures, which have been quite successful in generating coherent radiation at mid-infrared frequencies. Relevant issues, such as various depopulation intersubband scattering rates, the role of complex phonon spectra, and coherent vs. incoherent tunneling are discussed in details. Optically pumped sources, including optical parametric amplifiers, and both intersubband and interband pumped THz emitters, are also investigated for their feasibility in generating coherent THz radiations.

Key words: THz (Terahertz), intersubband, quantum wells, quantum-cascade lasers, LO-phonon, electron-electron scattering

1. Introduction

Terahertz (1–10 THz, or 4–40 meV, or 30–300 μm) frequencies are among the most underdeveloped electromagnetic spectra, even though their potential applications are promising for spectroscopy in chemistry and biology, astrophysics, plasma diagnostics, remote atmospheric sensing and imaging, noninvasive inspection of semiconductor wafers, and communications. This underdevelopment is primarily due to the lack of coherent solid-state THz sources that can provide high radiation intensities (greater than a milliwatt). The THz frequency falls between two other frequency ranges in which conventional semiconductor devices have been well developed. One is the microwave and millimeter-wave frequency range, and the other is the near-infrared and optical frequency range. Semiconductor electronic devices that utilize the transport of free charge carriers (such as transistors, Gunn oscillators, Schottky-diode frequency multipliers, and photomixers) are limited by the transit time and parasitic RC time constants. Consequently, the power level of these classical devices decreases as $1/f^4$, or even faster, as the frequency f increases above 1 THz. Semiconductor photonic devices based on quantum-mechanical interband transitions, however, are limited to frequencies higher than those corresponding to the semiconductor energy gap, which is higher than 10 THz even for narrow-gap lead-salt materials. Thus, the frequency range of 1–10 THz is inaccessible for conventional semiconductor devices.

Semiconductor quantum wells are human-made quantum-mechanical systems in which the energy levels can be designed and engineered to be of any value. Consequently, unipolar lasers based on intersubband transitions (electrons that make lasing transitions between subband levels) were proposed for long-wavelength sources as early as the 1970s.[1] This device concept has been realized in the successful development of quantum-cascade lasers (QCL) at mid-infrared wavelengths.[2] Recent development has extended the operating wavelengths of the QCLs to as long as 24 μm.[3] These achievements provide a great inspiration for the development of intersubband lasers in the THz frequencies below the *Reststrahl* band.

Free-carrier absorption increases at long wavelengths as λ^2, which could cause a significant cavity loss at the THz frequencies. By using thick ($\geq$10 μm) active regions or metallic waveguides for mode confinement, in combination of a low doping concentration ($<10^{16}/cm^3$), the cavity loss can be reduced to below 50 cm^{-1}, as verified recently in experiments.[4] Thus, the key to achieve lasing is to obtain a sufficient level of gain to overcome this moderate level of cavity loss.

The intersubband emitters are known to have a large joint density of states, because the two subbands, for example E_3 and E_2, track each other in the k-space. Thus electrons emit photons at the same energy regardless of their initial momentum if nonparabolicity is ignored. Therefore, the peak gain is related to the inverted population density $\Delta n = n_3 - n_2$ in a simple linear fashion, that is,

$$g = (\Delta n/t)(2e^2\omega/\hbar\varepsilon_r^{1/2}\varepsilon_o c)\, z_{ij}^2/\Delta f. \quad (1)$$

In Eq. (1), t is the thickness of the mode confinement region, and thus $\Delta n/t$ is the three-dimensional inverted population density within t. z_{ij} is the radiative dipole moment between the two subbands, and Δf is the FWHM linewidth of spontaneous emission. From Eq. (1), it is straightforward that a large peak gain can be achieved by a large dipole moment z_{ij}, a narrow emission linewidth Δf, and an appreciable level of population inversion Δn. The optimizations of the first two parameters are usually closely related, as a large dipole moment (accomplished by a strong spatial overlap of the two subband wavefunctions) tends to yield a narrow emission linewidth. Measured emission linewidth as narrow as 0.7 meV has been achieved with the calculated dipole moment greater than 50 Å.[5,6] Even with a moderate level of population inversion of $\Delta n \approx 10^9/cm^2$, the estimated peak gain will be greater than 100 cm^{-1}, which should exceed the cavity loss by a comfortable margin. Therefore the main challenge in the development of THz intersubband lasers is to achieve population inversion between two narrowly separated subband levels.

In this chapter, we review our recent work on the development of intersubband THz emitters. In Section 2, we will discuss our efforts in developing electrically pumped THz emitters, which include two types of structures. One utilizes electron-LO-phonon scattering, and the other utilizes resonant tunneling to depopulate the lower radiative level in order to achieve population inversion. Related issues, such as the role of interface and confined phonon modes, coupling between subbands near anticrossing (or resonance), and rate-equation analysis will also be discussed. In Section 3, we will review our investigations of optically pumped intersubband THz sources, including both intersubband-pumped and interband-pumped structures.

2. Electrically pumped intersubband THz emitters

Figure 1 illustrates schematics of emitters based on intersubband transition. Fig. 1(a) illustrates a scheme where the intersubband radiative transition takes place within one quantum well. This scheme is known as "intrawell" transitions. Fig. 1(b) illustrates a scheme where the intersubband transition takes place between two wells, which is known as "interwell" transitions. The intrawell scheme is conceptually straightforward and it has the advantages of a larger radiative dipole moment and a narrower emission linewidth. The interwell scheme, on the other hand, has the advantage that it allows the use of electron-LO-phonon scattering to depopulate the lower radiative state. We have made detailed investigations on both schemes.

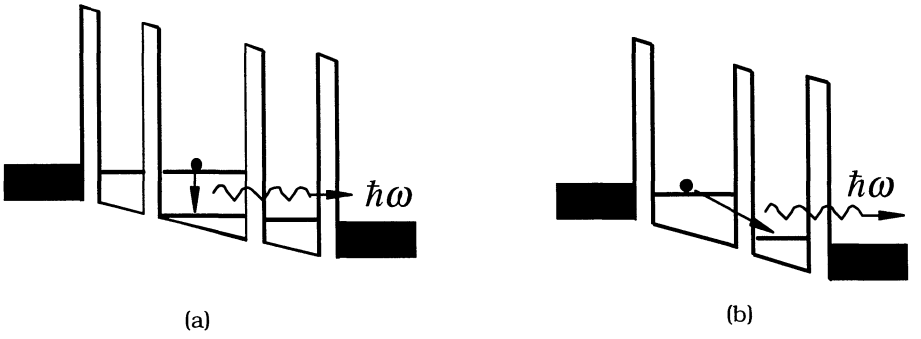

Figure 1. (a) Intrawell scheme of intersubband-transition lasers. (b) Interwell scheme of intersubband lasers.

2.1 THz emitters using electron-LO-phonon scattering for depopulation

Following the design principle of the original QCLs, we have designed intersubband THz emitters based on a three-level system. The top two subband levels, E_3 and E_2, form the radiative pair, while the ground state E_1 is at $\geq \hbar\omega_{LO}$ below E_2. Since it is energetically allowed, the fast electron-LO-phonon $E_2 \rightarrow E_1$ scattering will help to keep the population in E_2 low, and therefore maintain a population inversion between E_3 and E_2. However, because $E_3\text{-}E_2 < E_2\text{-}E_1 \geq \hbar\omega_{LO}$ for THz emitters, it is difficult to implement this three-level system based on an intrawell transition scheme, in which both E_3 and E_2 are primarily located in a single well. The bottom of this well would have to be raised relative to the rest of the structure so that $E_2\text{-}E_1 \geq \hbar\omega_{LO}$. Raising the bottom of the well would require adding aluminum to the well material GaAs, which would cause a significant alloying scattering and result in a broad emission linewidth.

Our design of the three-level systems is based on a scheme that the radiative transition takes place in a coupled double-well structure. A third well, which is much wider than the two wells, contains the ground-state level E_1. In our first design, the wavefunctions of E_3 and E_2 are primarily localized in separate wells, thus the $E_3 \rightarrow E_2$ transition is spatially diagonal. This design offers the advantage of a high selectivity in

injection into E_3 and removal from E_2, because of the spatial separation of the two wavefunctions. However, the diagonal nature of the radiative transition is quite sensitive to scattering due to interface roughness and alloy in the barrier, and thus the emission showed rather broad spectra ($\Delta f \sim$ 3-5 THz).[7]

It is well known that in a coupled double-well structure, the wavefunctions of the two lowest levels are spatially extended with a strong overlap at the anticrossing. Because of this spatial overlap, both levels are subject to the same interface and alloy scattering, and thus the emission linewidth of radiative transition between the two levels is reduced. In an improved structure, whose band structure and wavefunctions are shown in Fig. 2, we have taken advantage of this feature to enhance the strength of the radiative $E_3 \rightarrow E_2$ transition.[8]

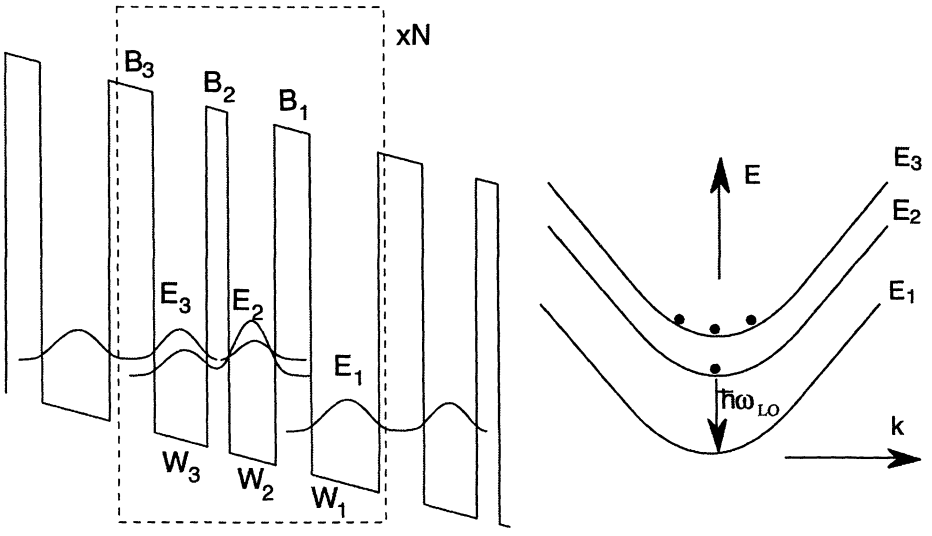

Figure 2. Schematic of a three-level system based on a triple quantum-well structure shown inside the dashed box. On the right is the dispersion relation between the energy and the transverse momentum.

In the structure shown in Fig. 2, the core is a three-well module of GaAs/$Al_{0.3}Ga_{0.7}As$ heterostructures (inside the dashed box), with three barriers B_1 (4.5 nm), B_2 (2.8 nm), B_3 (5.6 nm) and three wells W_1 (8.8 nm), W_2 (5.9 nm), and W_3 (6.8 nm). The collector barrier B_1 is center δ-doped at a level of $6\times10^{10}/cm^2$ in order to provide dynamic charges. Under the designed bias of 51 mV per module, the ground state E_1' (not shown) of a previous module is aligned with E_3. Thus, the upper level E_3 can be selectively populated via resonant tunneling. At this bias, the energy separation $E_{32} \approx 11$ meV (corresponding to 2.67 THz), and the dipole moment $z_{32} \approx 30$ Å. The energy separation $E_{21} \approx 40$ meV $\geq \hbar\omega_{LO}$, enabling electron-LO-phonon $E_2 \rightarrow E_1$ scattering for depopulation.

DC transport measurement confirmed our design. Fig. 3 shows the I-V curve and the differential conductance of a MQW structure with 30 modules. The device is cooled to ~5 K. The current increases monotonically with the bias below 2 V. The conductance

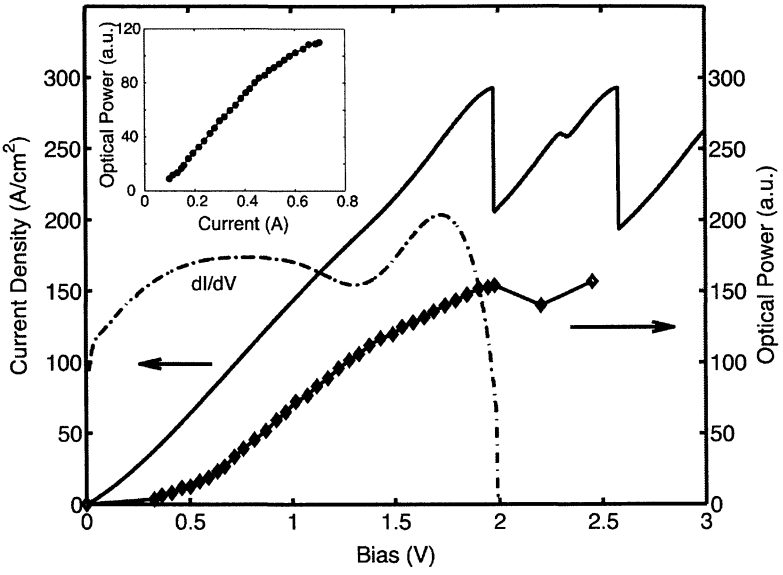

Figure 3. Measured dc current density and differential conductance versus the bias voltage of a THz emission device with 30 triple-well modules. The conductance peaks at the designed bias of ~1.7 V with a current density of 254 A/cm^2. Also plotted are the measured THz emission power versus bias and current (inset).

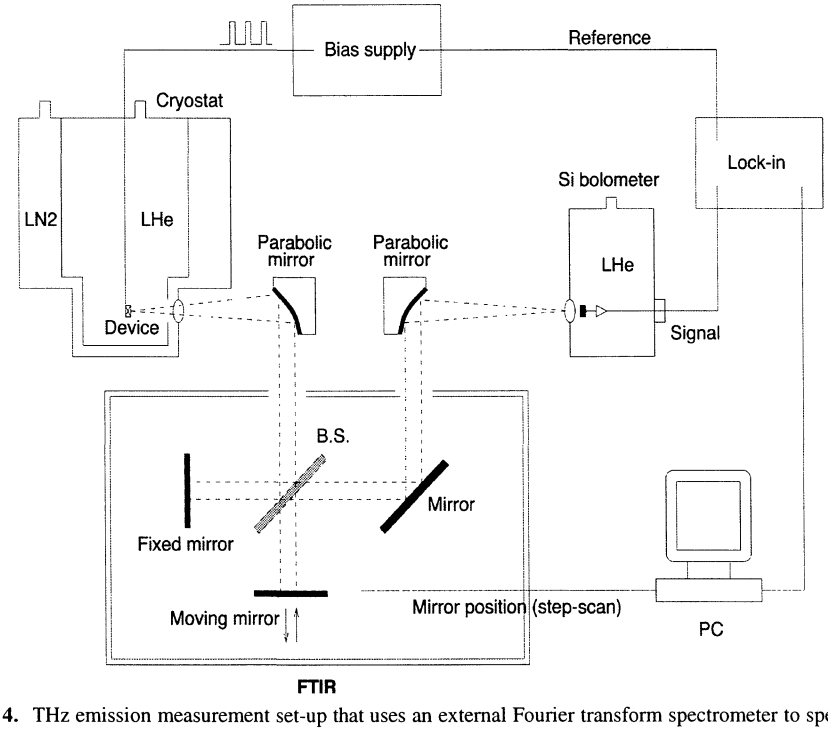

Figure 4. THz emission measurement set-up that uses an external Fourier transform spectrometer to spectrally resolve the emitted THz signals.

peaks at 1.7 V, which is close to the designed bias (51×30 mV) with the extra voltage likely due to the contact resistance. The conductance reaches its maximum at this bias due to the resonant tunneling of the E_1'→E_3 alignment.

In order to measure the intersubband THz emission and resolve its spectra, we constructed a set-up that included a Fourier transform infrared spectrometer (FTIR). The system's schematic is shown in Fig. 4. We have improved this system and perfected our measurement techniques so that THz emission measurements can be routinely performed on our emitters with output power levels of only several pW.

Our emission spectra reveal a clear peak due to the $E_3 \rightarrow E_2$ intersubband emission. A representative spectrum taken at 5-K device temperature is shown in Fig. 5(a), which was taken at the designed bias of 1.6 V (~30×51 mV). The measured peak frequency of 2.57 THz (10.6 meV) is close to the designed value of 11.3 meV. The FWHM linewidth is as narrow as 0.47 THz (1.9 meV). In order to verify the intersubband origin of the measured emission spectra, we have measured emission spectrum at a high bias of 4.0 V at which the energy levels are severely misaligned. The spectrum is shown in the inset of Fig. 5(a), and it bears little resemblance to the main figure.

Spectra were also taken with the cold stage cooled with liquid nitrogen to 80 K. One taken at a bias of 1.6 V is shown in Fig. 5(b). The main peak is essentially the same as the one measured at 5 K, with a slightly broader linewidth of 0.52 THz (2.14 meV). The linewidth measured at 80 K is expected to be similar to that at 5 K, since nonparabolicity is negligible for THz intersubband emitters. Nevertheless, our experimental verification is encouraging for the development of intersubband THz sources at elevated temperatures.

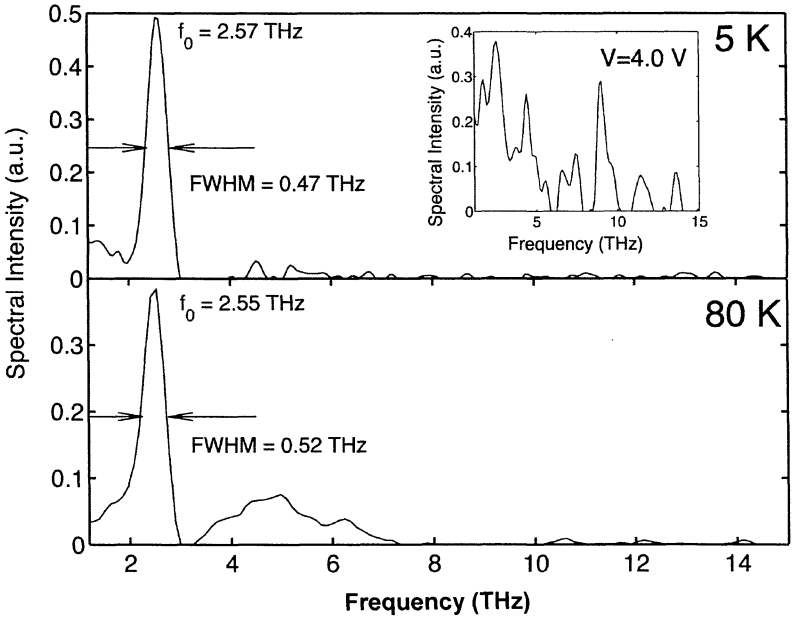

Figure 5. Spectrally resolved THz intersubband spontaneous emission taken at (a) 5-K and (b) 80-K bath temperature under 1.6-V bias. The inset shows the spectrum for 4.0-V bias, clear evidence that emission results from intersubband transitions.

2.2. Role of interface and confined phonon modes

Just like the electronic wavefunctions forming discrete subbands in MQW structures, phonon spectra also become discrete, forming spatially localized interface and confined modes. Despite this parallel analogy, bulk LO-phonon mode has been used to calculate the scattering times in QCLs. This practice may be justified for mid-infrared QC lasers, in which E_3-E_2 >> $\hbar\omega_{LO}$, so that the sum-rule yields the same result as obtained from using the bulk mode. However, as Dutta and Stroscio recently pointed out,[9] such a practice may be questionable for THz intersubband lasers, because E_3-E_2< $\hbar\omega_{LO}$ and E_2-E_1≈$\hbar\omega_{LO}$.

We have investigated the role of the complex phonon spectra on the intersubband scattering rates.[10] In the model used in our calculations, the phonon modes are described by the potential $\phi(\mathbf{r})$ resulting from the polarization field created by atomic displacements in a polar semiconductor. Each material layer of index i is described by a dielectric function $\varepsilon_i(\omega)$ as given by the Lyddane-Sachs-Teller relations, which vanishes at the LO-phonon frequencies. For lattice vibrations, since there are no free charges, the phonon potential must satisfy $\varepsilon(\omega)\nabla^2\phi(\mathbf{r}) = 0$. Two types of solutions exist: interface modes for which $\nabla^2\phi(\mathbf{r}) = 0$, and confined modes for which $\varepsilon(\omega) = 0$.

For the confined modes, $\varepsilon(\omega) = 0$ and therefore $\omega = \omega_{LO}$, where ω_{LO} is the bulk LO-phonon frequency in the layer of interest. Since ω_{LO} changes at the heterointerfaces, the potential must vanish there, and $\phi(\mathbf{r})$ can be described in terms of sine wave modes in z. A representative potential of several confined phonon modes is shown in Fig. 6. For the interface modes, $\varepsilon(\omega)\neq 0$, and the modes have frequencies $\omega\neq\omega_{LO}$, and the phonon frequencies depend on the transverse momentum $\mathbf{q}$. The potential solution is a linear combination of exponential terms peaked at the interfaces, hence the name of "interface mode". For our GaAs/AlGaAs quantum-well structures, there are usually two "GaAs-like" and one "AlAs-like" modes associated with each GaAs/AlGaAs interface. Thus, for the six interfaces in our triple-well structures shown in Fig. 2, there are a total 18 interface modes. A representative dispersion relation and potential profile of the interface phonon modes is shown in Fig. 7. The total scattering rate is the sum of the contributions from these 18 interface modes and all the confined modes (30 lowest confined modes were used in our calculations with the contributions from the higher modes negligible).

We used the transfer matrix approach[11] to account for the electromagnetic boundary conditions and obtain the mode potentials and dispersion relations for the interface modes. As it turns out, the 12 "GaAs-like" modes are clustered around 33-36 meV, close to the bulk GaAs LO-phonon energy. The 6 "AlAs-like" modes are clustered around 45-47 meV, close to the bulk AlAs LO-phonon energy, as illustrated in Fig. 7(a). Special care was taken to ensure a proper normalization of each mode, which was verified by limiting cases.[10]

In order to address the key issue raised in Ref. [9], namely the optimum subband separation E_{21}, we have calculated the maximum total scattering rate as a function of E_{21}, as shown in Fig. 8. The rate shows two peaks, one at ~35 meV due to the "GaAs-like" modes and the other at ~47 meV due to the "AlAs-like" modes. As a comparison, we also include the scattering rate calculated using the bulk GaAs LO-phonon mode. It is clear that the scattering rate is ~30% lower than the bulk mode if E_{21} ~ 36 meV, because of the exclusion of the "AlAs-like" modes. However, increasing E_{21} to ~47 meV does not increase the total scattering rate appreciably. This is because that at E_{21} ~ 47 meV, even

though all the phonon modes participate in the scattering, the rapid decrease in the strength of the "GaAs-like" modes away from their resonance (at ~36 meV) diminishes most of the benefit gained from including more active phonon modes.

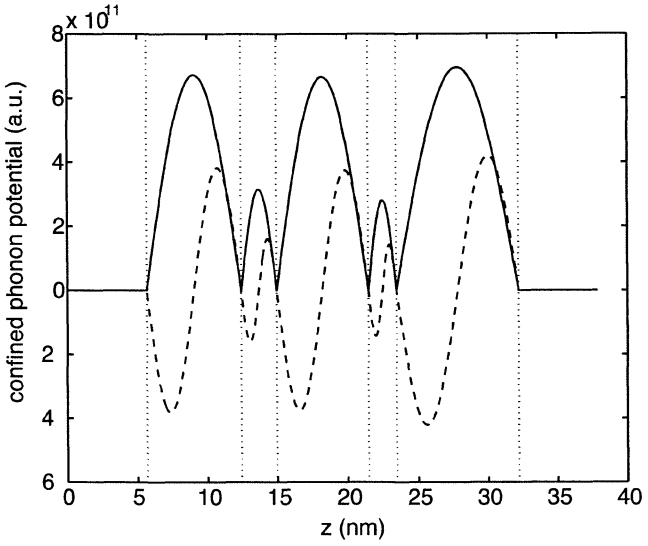

Figure 6. Phonon potentials for the confined "GaAs-like" modes for m = 1(solid lines) and m = 2 (dashed lines) at $\mathbf{q}$ = 0.3 nm^{-1}. The vertical lines represent heterointerfaces.

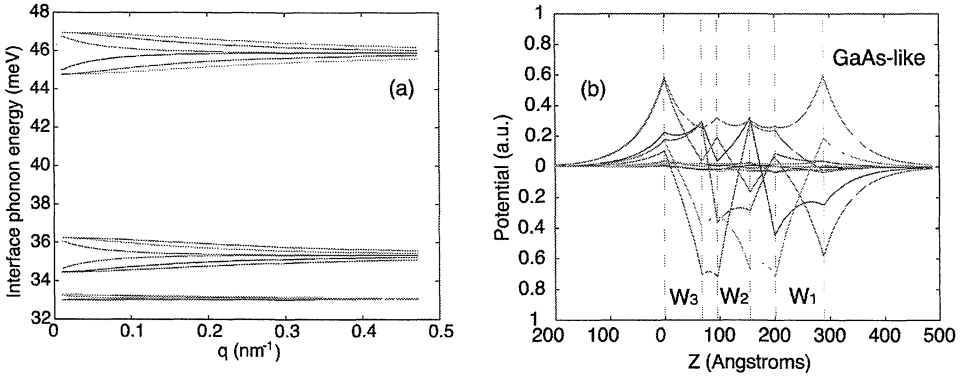

Figure 7. (a) Dispersion relation of all the 18 interface modes; (b) phonon potential profiles of the 12 "GaAs-like" interface modes associated with our triple quantum-well device.

In Fig. 9, we plot the key figure of merit $\tau_3(1 - \tau_{21}/\tau_{32})$, which is proportional to the population inversion Δn_{32}, as a function of the scattering time τ_{32}. As E_{21} increases from 36 to 47 meV, the increase in Δn_{32} is marginal at a given τ_{32}. Even this marginal increase should be taken with a grain of salt. As E_{21} increases from 36 to 47 meV, there will be an additional 11 meV energy dissipation per electron. This extra energy dissipation will further raise the electronic temperature. As a result, τ_{32} decreases because of LO-phonon scattering of hot electrons. Fig. 9 shows that a reduction in τ_{32} could undo any advantage

gained by increasing E_{21} to 47 meV. The conclusion from our analysis is that in electrically pumped THz intersubband emitters, because the barriers are thin and Al concentrations are low ($x \leq 0.3$), the contribution from the higher -energy "AlAs-like" modes only barely make up for the loss in the strength of "GaAs-like" modes. Thus, increasing E_{21} from 36 to 47 meV will only yield at the best a marginal (if any at all) improvement in population inversion Δn_{32}. For optically pumped intersubband THz lasers, however, because of thicker barriers with high Al concentrations ($x \geq 0.4$) and relatively narrow wells, the influence of the AlAs-like modes will be stronger; therefore the benefit of setting $E_{21} \sim 47$ meV may be more significant, as suggested in Ref. [9]. A recent development of an optically pumped intersubband Raman laser may have provided evidence that suggests important contributions of the AlAs-like interface modes to the intersubband scattering process.[12]

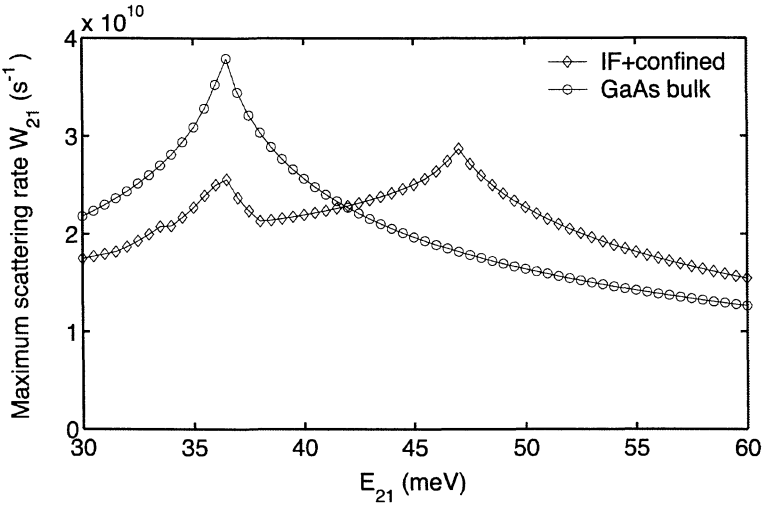

Figure 8. Maximum scattering rate versus subband separation E_{21} for the three-level structure shown in Fig. 1. Maximum scattering rate calculated with GaAs bulk modes is present for comparison.

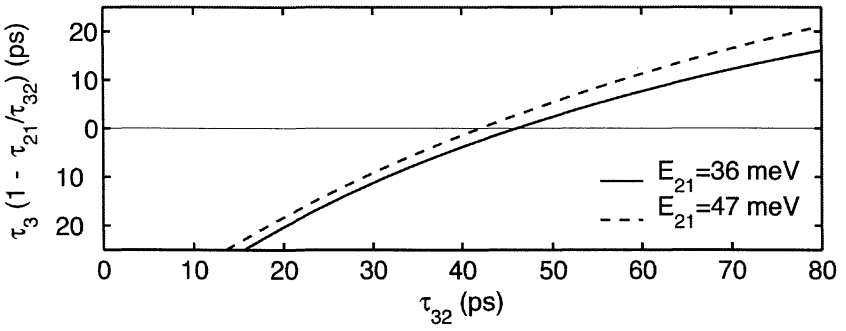

Figure 9. Plot of the quantity $\tau_3(1-\tau_{21}/\tau_{32})$, which is proportional to the population inversion Δn_{32}, versus the lifetime τ_{32} for the structure shown in Fig. 1.

2.3. Intrawell THz emitters using resonant tunneling for depopulation

Fig. 10(a) shows the calculated band diagram of another type of THz intersubband emission structure that we investigated recently.[6] In this structure, the radiative transition takes place between two subband levels primarily located in one quantum well. We consider this scheme as "intrawell" as opposed to the interwell scheme discussed earlier. It is well known that the intrawell scheme yields a larger dipole moment and a narrower emission linewidth, because the subband separation is less sensitive to impurity and interface roughness scattering.[5]

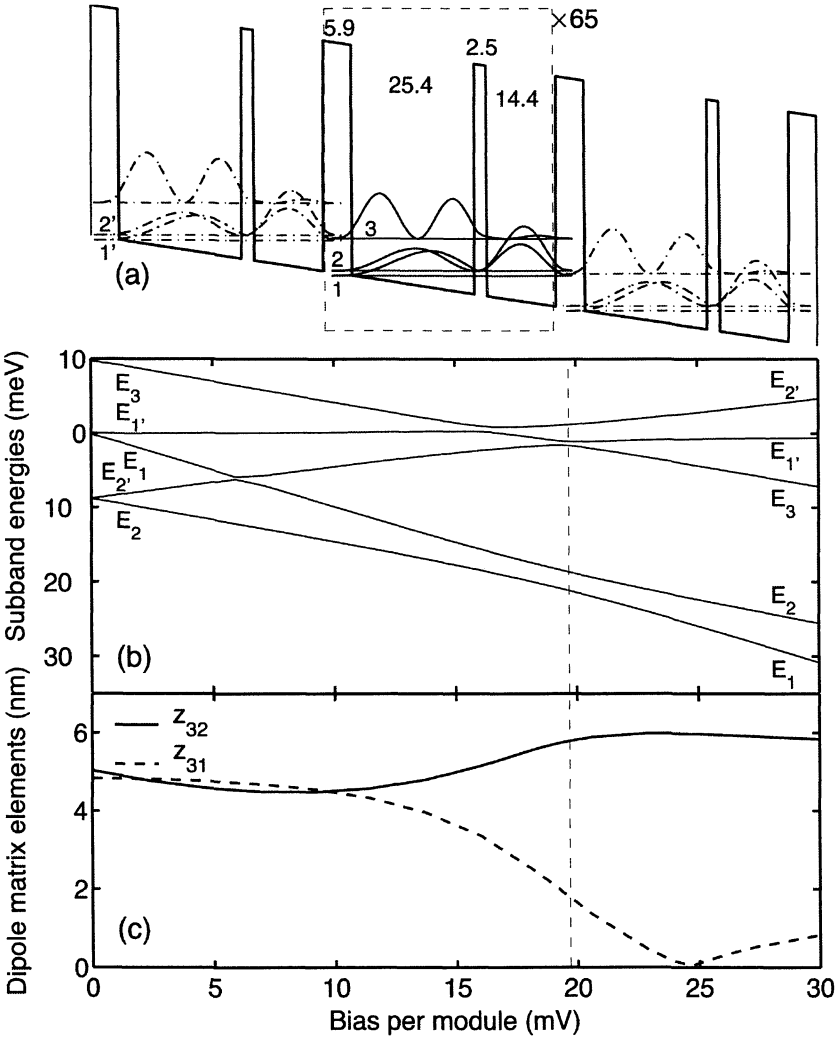

Figure 10. (a) Computed conduction band profile and squared magnitude wavefunctions for the intrawell device. Plot of the (b) subband energies with respect to the injection level $n = 1'$, and (c) dipole matrix elements vs. applied bias. The dashed line in (b) and (c) indicates the designed operating bias.

The core of the structure shown in Fig. 10(a) is a coupled double-well module shown inside the dashed box. Sixty-five nominally identical modules are cascade connected. Under the designed bias of ~20 mV/module, the lower level E_2 in the wide well is aligned with the lowest level E_1 in the narrow well, which in turn is aligned with the upper level in the wide well of the following module. The radiative transition takes place between E_3 and E_2, which have a strong spatial overlap as can be seen in Fig. 10(a). The depopulation of E_2 is facilitated through "resonant tunneling" from E_2 to E_1, which deserves special attention and will be discussed in the following. The calculated dipole moment z_{32} is as large as ~6.0 nm at the designed bias (shown in Fig. 10(c)), as a result of the strong radiative coupling in this intrawell scheme.

Fig. 11 shows measured emission spectra taken at a bias of 1.5 V and 2.0 V, which are somewhat greater than the designed bias (65x20 mV ≈ 1.3 V). Both spectra show a clear peak at 21 meV (~5.04 THz) due to the 3→2 radiative transition, with a FWHM linewidth as narrow as 0.7 meV (0.18 THz). As expected, due to the intrawell nature of the radiative transition, the peak displays no appreciable Stark shift for the bias range of 0.8-2.25 V. The measured emission frequency is close to the calculated subband separation $E_{32} \approx 18.5$ meV, and the narrow linewidth indicates the high quality of the MBE growth.

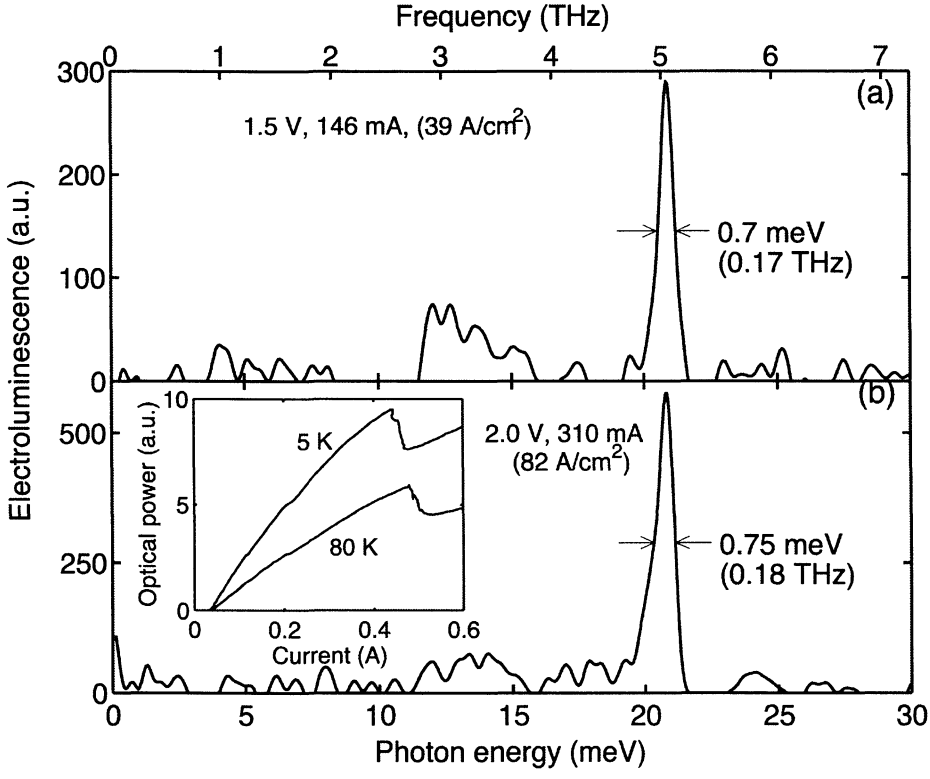

Figure 11. Electroluminescence spectra at 5 K for applied biases (a) V = 1.5 V and (b) V = 2.0 V. The inset displays the emitted optical power vs. current.

The term "resonant tunneling" usually refers to electron transport between two subband levels close in energies. There has been a long debate on whether this process should be analyzed as intersubband scattering between two spatially extended wavefunctions (the scenario of coherent resonant tunneling), or as tunneling between two spatially localized states (the scenario of incoherent sequential tunneling). This question is not merely academic, but is crucial for the successful development of intersubband THz lasers, as the two transport mechanisms yield very different depopulation rates. For coherent resonant tunneling, the electron transport is facilitated by fast (<1 ps) electron-electron intersubband scattering. For incoherent sequential tunneling, the depopulation rate is determined by the barrier transparency, which can be much slower than the first scenario.

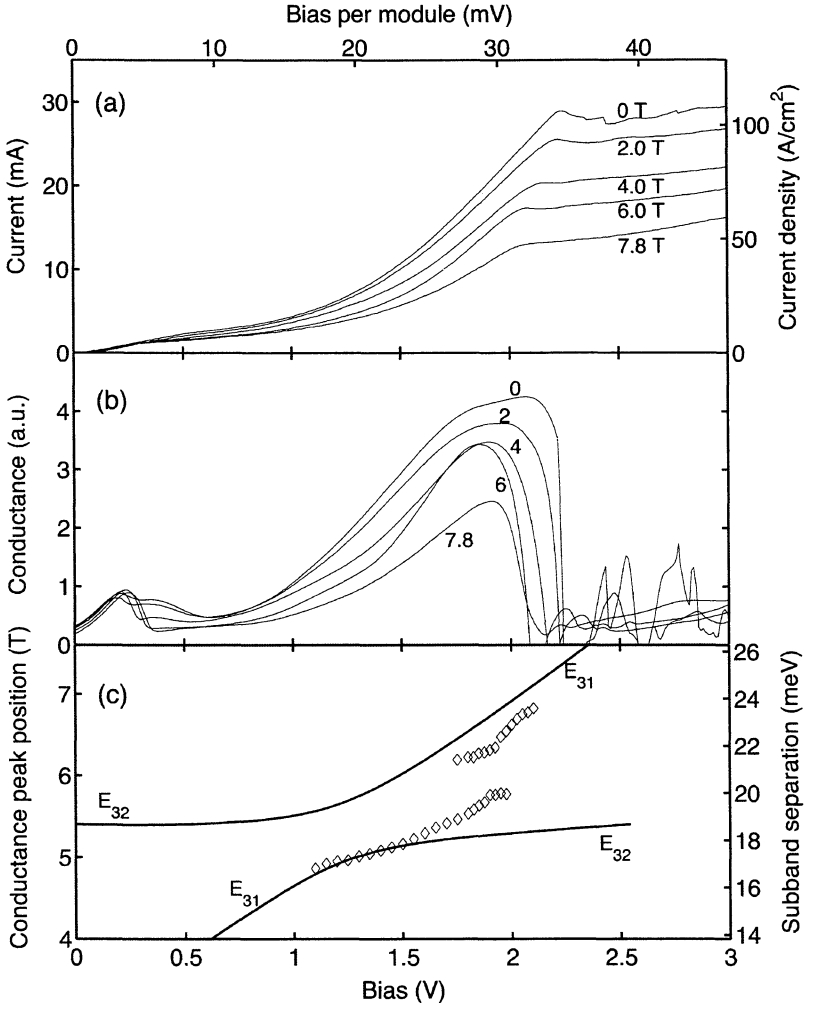

Figure 12. Current (a) and conductance (b) for several values of applied magnetic fields at 4.2 K. (c) Position of $\Delta I = 2$ peaks in *G-B* plots and associated energy difference near the anticrossing of subband 2 and 1. The solid lines are the corresponding calculated energy difference E_{32} and E_{31}.

In the coherent picture, the energy difference between any pair of two subbands has a finite minimum value, known as the anticrossing gap Δ, which characterizes how strongly the two subbands are coupled. In contrast, in the incoherent scenario, the two subband wavefunctions are spatially localized in different wells. Their energy levels can be degenerate and thus may be arbitrarily close at resonance. Based on the coherent model, we have calculated $\Delta_{21} = \min |E_2\text{-}E_1| \approx 2.5$ meV. Even though current -field (*I-B*) magneto-tunneling spectroscopy has been successfully used to resolved subband separations of ~20 meV,[13,14] the resolution of the anticrossing gaps of only a few meV requires the measurement of conductance $G = dI/dV$ to enhance the energy resolution and sensitivity.

For magnetotransport measurements, devices were processed into 150×150 μm^2 mesas, and mounted in liquid helium inside a magnet dewar. Magnetic fields up to 8 T were applied along the growth direction (parallel to current flow). Current-voltage and conductance-voltage characteristics are shown in Fig. 12.

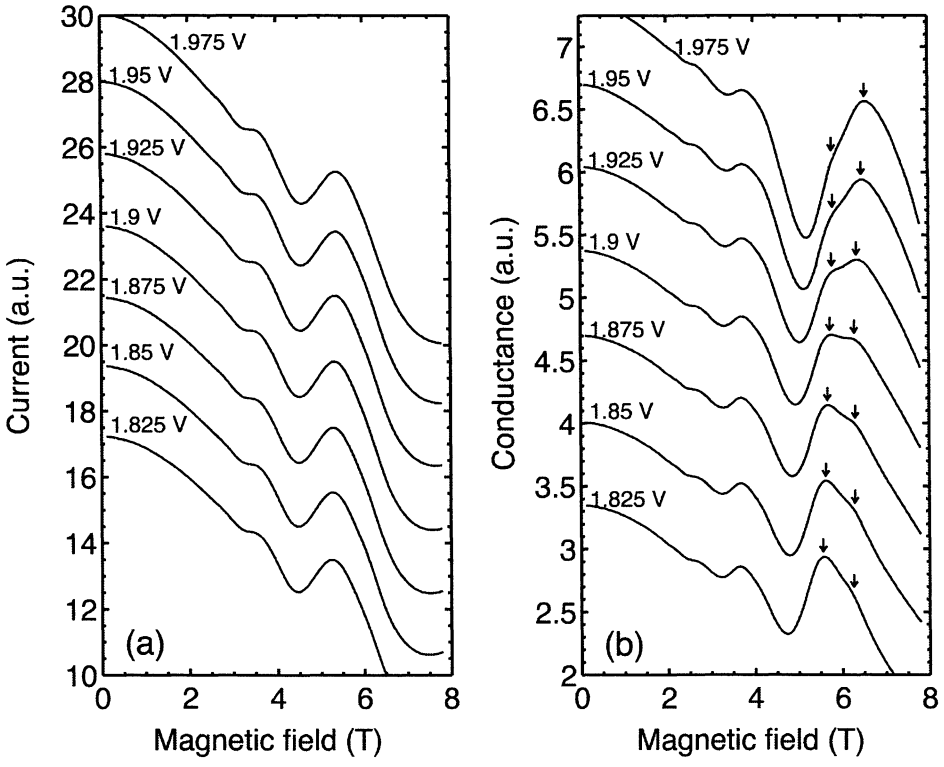

Figure 13. Current (a) and conductance (b) vs. magnetic field (**B**||**J**) for several applied biases. The curves are offset for visibility. The arrows in (b) indicate the resonance peaks that correspond to 2-1 anticrossing.

At $B = 0$, the conductance curve flattens at 1.8-2.1 V, as $n = 3$ becomes aligned first with $n = 2'$ and then with the injector state $n = 1'$. At 2.25 V, $n = 1'$ becomes severely misaligned with $n = 3$, and a negative differential resistance (NDR) occurs. While this bias voltage is somewhat greater than the calculated design bias of 1.3 V, the difference

is partially due to parasitic series resistance. As B is increased from 0 to 7.8 T, the current decreases due to the reduction in phase space for intersubband scattering. Additionally, the NDR shifts to lower voltages with increasing B. The formation of the Landau levels sharpens the density of states, and thus less misalignment of the n = 1' and 3 is tolerated before the device enters a NDR region.

Fig. 13 shows both *I-B* and *G-B* curves measured in a voltage range near the E_2-E_1 anticrossing. For example, at V = 1.90 V, the *I-B* maxima corresponding to the change of Landau level index Δl = 2,3,4 are seen at 5.47, 3.64, and 2.73 T, which correspond to an energy separation of 19 meV. This value of energy separation is close to the calculated intersubband spacing. While the peaks in the *G-B* curves generally mirror those in the *I-B* curves, however, at V>1.8 V the *G-B* data reveal the more complicated structure of an anticrossing between two Δl = 2 peaks (indicated by the arrows in Fig. 13(b)). As the bias is increased, the magnitude of the lower-energy peak decreases while that of the higher-energy peak increases. The limited resolution at B~4 T largely obscures much of the anticrossing effect for the Δl =3 peaks.

The dependence of these Δl = 2 conductance peaks on bias is shown in Fig. 12(c), and it displays a typical anticrossing behavior between a Stark shifted peak and another fixed at ~6.0 T (~21 meV). This 21-meV peak corresponds to the 3→2 transition, which agrees well with the emission data shown in Fig. 11. The Stark shifted peak corresponds to the 3→1 transition, as the two wavefunctions are spatially more separated than those of E_3 and E_2. At 1.9 V, the peaks in *G-B* are minimally separated by 0.5 T, which corresponds to an anticrossing gap of 1.7 meV. This value agrees reasonably well with the calculated value of 2.5 meV, which was calculated assuming a totally coherent scenario. In the presence of scattering, which is unavoidable in any real devices, the minimum energy separation of two subbands should be somewhat smaller than the calculated value based on a coherent model. In addition, the overall dependence of the conductance peaks on the bias agree reasonably well with the calculated energy differences E_{31} and E_{32}, as shown in Fig. 13(c). Our work shows that in the particular structure shown in Fig. 10(a), the E_2→E_1 depopulation should be modeled as intersubband scattering between two spatially extended states.

2.4 Transport issues of electrically pumped THz intersubband emitters

The results presented in Sections 2.1 and 2.3 showed unambiguous evidence of intersubband emission at THz frequencies with good characteristics (narrow linewidths and fidelity at elevated temperatures). The key issue in achieving lasing now is in a careful design and implementation of a transport scheme, involving injection into the upper radiative subband, intersubband scattering, and removal from the lower radiative subband level, in order to achieve an appreciable degree of population inversion between the two radiative levels. In principle, all the above-mentioned transport processes should be correctly modeled as intersubband scattering, in order to obtain a quantitative measure of the relative rates of various processes.

Fig. 14 illustrates the scattering processes of several mechanisms. The radiative transition and electron-acoustic-phonon scattering are slow processes with the time scale longer than ~ns. Thus, they can be ignored in rate-equation analysis, although the

radiative transition rate is crucial in determining the spontaneous emission efficiency and gain of the active medium, and the electron-acoustic-phonon scattering is important in dissipating excess electronic energies. The processes due to electron-LO-phonon scattering and electron-electron scattering have some features that are unique for THz intersubband emitters. In contrast to mid-infrared QCLs, where the energy separation between the two radiative subband levels is always greater than the LO-phonon energy $\hbar\omega_{LO}$, thus electron-LO-phonon scattering is always energetically allowed. At THz frequencies, even though the subband energy separation is less than $\hbar\omega_{LO}$, however, hot electrons with excess kinetic energy will subject to electron-LO-phonon scattering. Clearly, this scattering process depends on the excitation level of the devices. Because of the long-range Coulomb interaction, the electron-electron scattering is inversely proportional to the square of the momentum (or the energy) involved. Thus, even though this process has been more or less ignored in the analysis of mid-infrared QCLs, it plays a crucial role in the intersubband scattering in THz intersubband emitters. As can be seen from the insets in both Fig. 3 and Fig. 11(b), the power-current relation is sublinear. In fact, the power-current (P-I) relation can be well described by a $P \propto I^{1/2}$ relation for the P-I curve shown in Fig. 11(b) at 5 K. This $P \propto I^{1/2}$ relation is a direct consequence of a lifetime reduction due to the electron-electron scattering at high injection levels. As $P \propto n_3$, $I \propto n_3/\tau_3$, and $\tau_3 \propto 1/n_3$, and hence the $P \propto I^{1/2}$ dependence.

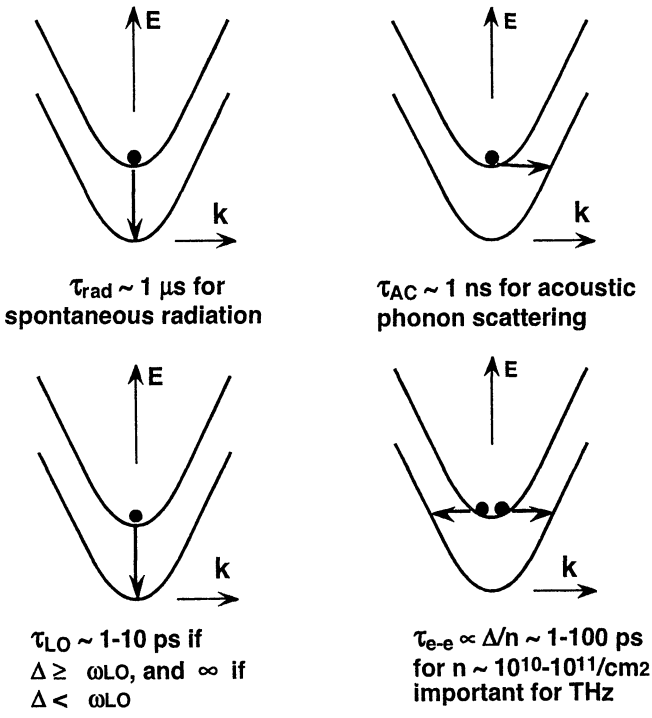

Figure 14. Schematics of various intersubband scattering processes, namely: radiative transition, electron-acoustic-phonon, electron-LO-phonon, and electron-electron scattering.

Clearly, the rate of electron-electron scattering depends on the populations of the involved subband (roughly proportional to the subband population), thus this scattering process also depends on the excitation levels. Both electron-LO-phonon scattering and electron-electron scattering rates increase with the excitation level. At high excitation levels (corresponding to high current densities and bias fields), the electronic temperature could be significantly higher than the lattice temperature, resulting in an increase of hot electron scattering by emitting LO-phonons. Also, at high injection levels, the increased electron population at the upper level increases the electron-electron scattering rate, resulting in a decrease of the injection efficiency. Both processes are detrimental for the establishment of a population inversion. Thus, a successful design of THz intersubband lasers cannot simply increase the injection level by increasing the doping concentrations and using thinner barriers. Rather, a delicate trade-off must be balanced between a sufficient injection level and not being overwhelmed by the two detrimental processes at high injection levels.

The mechanisms of depopulation of the lower radiative level is different for the two structures shown in Fig. 2 and Fig. 10(a). The first one (in Fig. 2) relies on electron-LO-phonon scattering, while the latter relies on electron-electron scattering. As a result, the rate analysis is quite different for the two structures. In the structure shown in Fig. 2, because of the large energy separation of E_2-$E_1 \approx 40$ meV, back filling process of 1→2 is negligible at cryogenic temperatures. In the structure shown in Fig. 10(a), however, E_2-$E_1 \approx 2$ meV, back filling is an important process. We analyze the two structures separately in the following.

THz emitters using electron-LO-phonon scattering for depopulation

In this structure, if we ignore the 1→2 back scattering, then the population inversion is given by:

$$\Delta n = n_3 - n_2 = \frac{J}{e}\frac{\tau_{31}}{\tau_{32}+\tau_{31}}\left(\tau_{32}-\tau_{31}\right) > 0, \text{ if } \tau_{32} > \tau_{31} \tag{2}$$

where τ_{ij} is the scattering time from *ith* to *jth* subband, and J is the injection current density. It is clear from Eq. (2) that a population inversion is achieved if $\tau_{32} > \tau_{31}$, regardless of other parameters. However, in order to achieve a large degree of population inversion, the ratio $\tau_{31}/(\tau_{31}+\tau_{32})$ should be optimized by making $\tau_{31} >> \tau_{32}$. The scattering time τ_{21} is mainly determined by electron-LO-phonon scattering, as the energy separation ΔE_{21} is designed to be close to the LO-phonon energy $\hbar\omega_{LO}$. In the particular structure shown in Fig. 2, because of the relatively thick barrier B_1, the lifetime τ_{21} is as long as ~27 ps (calculated using the bulk GaAs LO-phonon mode). τ_{32}, however, is mainly due to electron-electron scattering and LO-phonon scattering of hot electrons. Both processes depend on the injection levels and it is difficult to accurately calculate this scattering time. From the measured peak current density and designed doping concentration, we can estimate that τ_{32} to be ~20 ps, with a large uncertainty due to the uncertainty in doping concentration and nonspecular tunneling from 1' to 2. Given our later investigation on the electron-electron scattering time (~10 ps), we believe that it is unlikely that population inversion is achieved in the structure shown in Fig. 2, because of the long lifetime of τ_{21}. In principle, this problem can be solved straightforwardly by using a thinner barrier B_1,

which will yield a shorter lifetime τ_{21}. In practice, however, because of the strong spatial overlap of the wavefunctions of E_3 and E_2 that is needed to achieve a narrow emission linewidth and a large dipole moment, a short τ_{21} will result in a proportionally short τ_{31}, which will be detrimental in two ways. First, it will reduce the prefactor in Eq. (2), which will quantitatively reduce the degree of population inversion. Second and perhaps the worst, it will result in a significant parallel current channel due to the 3→1 scattering process. This parallel current channel will not contribute anything to the desired injection channel, but will generate additional heat that raises the electronic temperature. As a consequence, the LO-phonon scattering of hot electrons in E_3 will significantly shorten the scattering time τ_{32}, which could qualitatively destroy population inversion, as can be seen from Eq. (2).

The dilemma in the design of a suitable structure similar to that shown in Fig. 2 illustrates the competing requirements of a strong coupling between the two radiative subband levels and a selective coupling of one of them to a different level. For E_3, it is desirable that it is strongly coupled to the injector level E_1'. For E_2, it is desirable that it is strongly coupled to the ground-state level E_1. Meanwhile, it is desirable that E_3 has a minimum coupling with E_1, and E_2 has a minimum coupling with E_1'. The latter requires a high-quality interface, so that tunneling is mostly specular, and the simultaneous conservation of energy and transverse momentum reduces the E_1'→E_2 process at the designed bias. The former can be achieved by adding an additional buffer well between E_2 and E_1. This buffer well will largely block the E_3→E_1 process while still allowing a fast depopulation of E_2. We are actively pursuing this approach in our current investigation.

THz emitters using electron-electron scattering for depopulation

Because of the small energy separation $\Delta E_{21} \approx 2$ meV and thus electron -LO-phonon scattering is not energetically allowed, the depopulation of E_2 in structure shown in Fig. 10(a) relies on resonant tunneling. As discussed in Section 2.3, this process should be correctly modeled as electron-electron scattering between two spatially extended states E_2 and E_1. Because of the small energy separation of ΔE_{21}, the rate of electron-electron scattering is very fast (~1 ps, depending on the subband populations). Also, because of the small energy separation ΔE_{21}, the back filling process 1→2 is almost as likely as the forward scattering process of 2→1 at elevated temperatures. To the first degree of approximation, we model the two subbands E_2/E_1 as a coherent "doublet" that can be characterized by a single chemical potential μ. This model assumes that the intra-doublet scattering is much faster than the inter-doublet scattering, so that electrons in the doublet reach a quasi-equilibrium. The total electron density n is splited in three ways among the three subband levels E_3, E_2, and E_1, with the population on E_2 and E_1 determined by μ. In this simplistic model, from the measured current density (assuming the injection tunneling is specular), it is possible to estimate the relative subband populations if the lifetime on the upper subband level τ_3 is known.

Fig. 15 shows the result of a measurement that is intended to extract the value of lifetime τ_3. Since the emission power $P \propto n_3$, and the current density $J \propto n_3/\tau_3$, the ratio of the two is given by:

$$\frac{P}{J} \propto \tau_3 = \left[\tau_{ee}^{-1} + \tau_{LO}^{-1} \exp\left(\frac{E_{32} - \hbar\omega_{LO}}{k_B T} \right) \right]^{-1} \tag{3}$$

where τ_{ee} is the scattering time due to electron-electron scattering, and τ_{LO} is the scattering time due to electron-LO-phonon scattering when the electrons have sufficient kinetic energy on E_3 for LO-phonon scattering. τ_{LO} is calculated to be ~0.4 ps using the bulk GaAs LO-phonon mode. In Fig. 15, we plot measured *P/J* vs. 1/T. As can be seen from the figure, *P/J* decreases at high temperatures due to the lifetime reduction from LO-phonon scattering of hot electrons. *P/J* is flat at low temperatures with the level set by the electron-electron scattering, which is approximately temperature independent. From Fig. 15, we can infer the electron-electron scattering time to be approximately 17 ps. The current density and the upper-level population is related through $J = en_3/\tau_3$, or $n_3 = (J/e)\tau_3$. From Fig. 12(a), the peak current density $J \approx 100$ A/cm^2, which yields a upper-level population $n_3 \approx 1.1 \times 10^{10}$/cm^2. The total two-dimensional electron density is measured from a C-V measurement to be $N_D = n_1+n_2+n_3 \approx 2 \times 10^{10}$/cm^2. Thus, a population inversion $n_3 > n_2$ can be inferred from these measurements. However, devices with structures similar to that shown in Fig. 10(a) did not achieve lasing, even when they were integrated with low-loss THz cavities formed by metal waveguides. We suspect that the extracted value of τ_3 is much longer than its actual value, and consequently no population inversion is established in the structure. The reason for this discrepancy is unclear to us at the moment. A recent transport analysis based on a three-dimensional Monte Carlo simulation yielded a much shorter electron-electron scattering time (<10 ps) for a structure similar to the one shown in Fig. 10(a).[15] The same Monte Carlo simulation analysis correctly predicted the measured current density, illustrating its accuracy in analyzing various scattering processes. In collaboration with Prof. S. Goodnick at Arizona State University, we are currently developing our own Monte Carlo simulation package to further investigate the transport processes in various intersubband THz emitters.

Our investigations on the emission and transport properties of the two intersubband structures shown in Fig. 2 and Fig. 10(a) indicate that they show good radiative characteristics. However, further refinement in the design of their transport properties is needed to achieve a population inversion, while still preserving their good radiative characteristics. For the structure shown in Fig. 2, the key challenge is to achieve a short lower-level lifetime τ_2, while keep the upper-level lifetime τ_3 relatively long. This can be achieved by using additional buffer wells to reduce the coupling between the upper level E_3 and the ground state E_1. For the structure shown in Fig. 10(a), an obvious direction for improvement is to increase the injection current density J, as $n_3 = (J/e)\tau_3$. An increase in current density will increase n_3 and decrease $n_2 = N_D - (n_3+n_1)$, both are desirable changes to help establishing a population inversion $n_3 > n_2$.

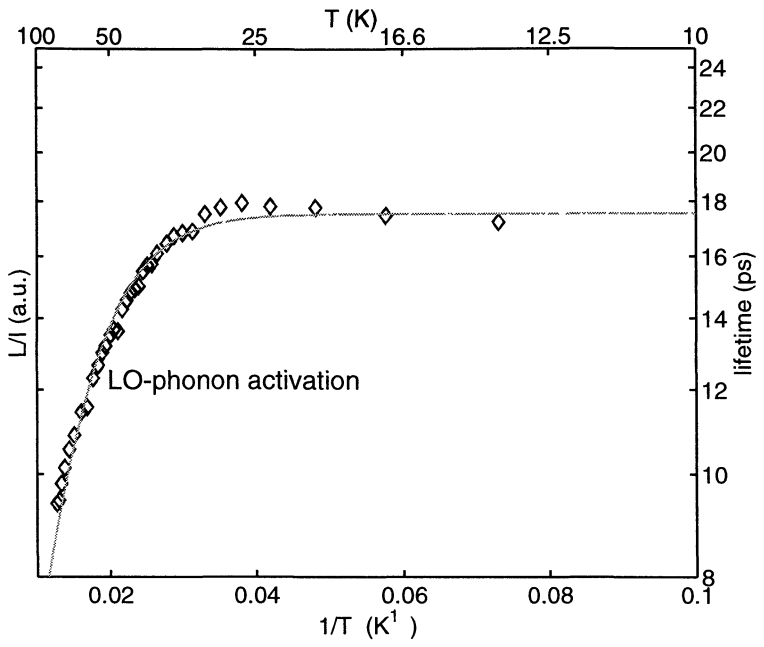

Figure 15. Measured light power/current (L/I) ratio, which is proportional to the lifetime of the upper level, as a function of the device temperature. The9 roll-off of L/I at high temperatures is due to thermally activated LO-phonon scattering. L/I is approximately constant at low temperatures, which gives a measure of the electron-electron scattering time scale of ~17 ps.

3. Optically pumped intersubband THz emitters

Although electrical pumping is preferred because of its simplicity in operations, optical pumping offers advantages in selectivity of pumping and simplicity in designs. Many types of lasers were first invented using optical pumping and then achieved electrical pumping only after the involved technology became mature. In parallel with our main effort in the development of electrically pumped intersubband THz lasers, we have also investigated the possibility of using optical pumping to achieve THz lasing. We summarize key results in this section.

3.1 Intersubband pumped THz optical parametric oscillators (OPOs)

We started our investigation of optically pumped THz sources with the development of optical parametric oscillators (OPOs). OPOs are commonly used near-infrared sources at wavelengths longer than ~1 μm where the frequency is below the bandgap energy of typical semiconductor diode lasers. They have the advantage of frequency tunability (by temperature or incident angle). Their operation requires a large nonlinearity in the dielectric constants ($\chi^{(2)}$) and phase-matching condition. Because of the large dipole moments associated with intersubband transitions, it has long been recognized that quantum-well structures possess large $\chi^{(2)}$ values at frequencies near the intersubband

resonances. Experimentally, it has been demonstrated that $\chi^{(2)}$ is as large as 10^{-6} m/V, which is orders of magnitude larger than the value for bulk GaAs materials.[16,17] It was this large nonlinearity associated with the intersubband transitions that motivated us to pursue the development of intersubband-pumped THz OPOs, whose schematic is illustrated in Fig. 16.

The active core of the device is a coupled double-well structure with three subband energy levels. The energy separation of these subband levels correspond to the frequencies of the pump ω_p, THz signal ω_S, and the idler ω_I. As a result, all these three beams are at resonance with intersubband transitions, yielding a large value of $\chi^{(2)}$ for the intended frequency down conversion process. Quasi-phase matching in this device can be achieved by applying different voltages on periodic placed electrodes, the resulting Stark shift could significantly reduce the value of $\chi^{(2)}$ in the region that the reverse OPO process takes place, thus extending the length of the active gain medium.

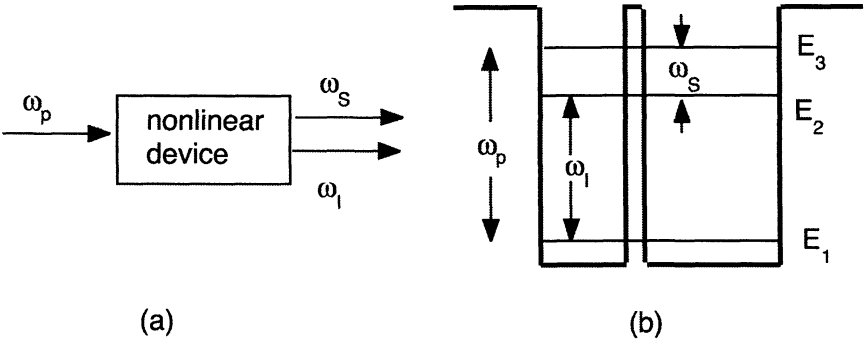

Figure 16. (a) Schematic of an OPO. (b) Its implementation using a coupled double-well structure involving three subband energy levels.

In a theoretical analysis, we have discovered that in contrast to near-infrared OPOs in which all the three beams suffer very little attenuation losses, the losses for the intersubband OPOs are heavy for all the three beams due to a large-value $\chi^{(1)}$ process that is associated with the large dipole moments in intersubband transitions. As a result of this heavy attenuation, plane waves are no longer good approximations to describe the three propagating beams. In other words, the momentum of each beam is no longer a good quantum number. Consequently, phase matching condition, which is the mathematical statement of momentum conservation, is no longer strictly required in a gain medium that the pump and idler beams suffer heavy attenuation.[18] This result could help to simplify the design and implementation of OPOs based on intersubband transitions. Using reasonable device parameters, we estimate that the threshold gain is ~50 cm^{-1}, which requires a pump power level of ~100 W. Such a pump power should be easily obtainable from a Q-switched CO_2 laser.

3.2 Intersubband optically pumped THz lasers

Both optically pumped lasers and OPOs are frequency down converters, which requires the use of nonlinear elements. Using the analogy and language of circuit elements, one utilizes a nonlinear reactance (OPOs) and the other one utilizes a nonlinear resistance (optically pumped lasers). For OPOs, the reactive nonlinear down conversion conserves both energy (through the Manley-Rowe relation) and momentum (through the phase matching condition). For optically pumped lasers, neither photon energy nor photon momentum is conserved, reflecting their dissipative nature in the down conversion process. In practice, since no phase matching condition is required, optically pumped lasers are much easier to operate than OPOs, as the pumped beam can be aligned arbitrarily with respect to the output signal beam. At near-infrared wavelengths ($\lambda > 1$ μm), there are no real energy levels with long lifetimes available in commonly used semiconductor materials. Thus, OPOs that utilize the reactive nonlinearity (associated with virtual states) are commonly used. In the case when real energy levels are available, optically pumped lasers have always been the choice of approach for their easy operations. For the intersubband structure depicted in Fig. 16(b), clearly there are real energy levels with sufficiently long lifetimes, thus optically pumped lasers should be easier to develop than OPOs. It was this analysis that led us to the path of developing optically pumped THz lasers by intersubband pumping.

Unlike OPOs, in which all the three beams at ω_p, ω_S, and ω_I play important roles in the outcome of the devices, in optically pumped lasers only the radiative pair involves in the optical transition and the rest of the states provide nonradiative scattering channels for achieving population inversion. Thus, OPOs will only need three energy levels while optically pumped lasers will need a minimum three levels but often more levels for better performance. We have investigated intersubband structures with three-, four-, and five-levels, with the main focus on the four-level structures.[19,20] Fig. 17(a) shows a intersubband structure with three-levels, and Fig. 17(b) shows a structure with four-levels.

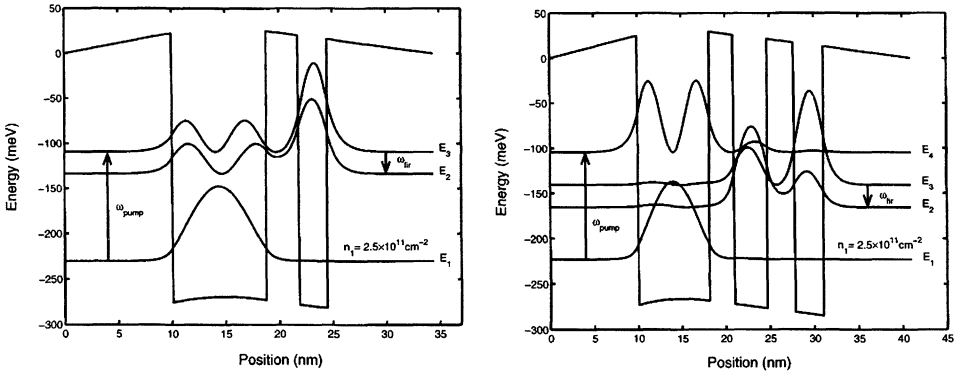

Figure 17. (a) Schematic of a three-level intersubband system using a coupled double-well structure. (b) Schematic of a four-level intersubband system using a coupled triple-well structure.

The three-level system is conceptually simpler and the analysis is straightforward. The radiation efficiency η is given by:

$$\eta_{3L} = \sigma_{31} n_1 \frac{\omega_{32}}{\omega_{31}} \frac{\tau_3^{tot}}{\tau_{32}^{rad}} \tag{4}$$

where σ_{31} is the pump cross section for the 1→3 excitation, n_1 is the electron density on E_1, ω's are intersubband transition frequencies, and τ's are intersubband transition times. With reasonable device parameters, we estimate that the (spontaneous) radiation efficiency for the three-level system is ~4×10^{-10}, which is quite low, largely because of the short lifetime τ_3 as a result of many fast nonradiative relaxation channels for electrons to come down from E_3. It is difficult to significantly improve η_{3L} by modifying the design of the three-level system. Increasing the doping concentration to increase n_1 will cause a greater level of free-carrier absorption. Increasing the cross section σ_{31} will also not work. The resulting stronger overlap between wave functions in levels E_1 and E_3 leads to a faster LO-phonon scattering rate $1/\tau_{31}$. It is also difficult to increase the Manley-Rowe factor ω_{32}/ω_{31} because the only practical pump source (a CO_2 laser) operates in a narrow frequency range ~110-135 meV.

Here is where the power of quantum well as an "artificial atom" comes to play. With quantum wells we have the ability to design wave functions and phonon scattering rates. However, the simple three-level scheme does not give us enough flexibility to take advantage of this power. By using more levels, for example a four-level system, we could tailor the wave functions to achieve a longer upper-level lifetime while still preserving a large pump cross section. Fig. 17(b) illustrates the structure of a four-level system. In this structure, electrons are optically pumped from E_1 to E_4. E_4-E_3 is designed to be close to $\hbar\omega_{LO}$ so that electrons quickly decay from E_4 to E_3. The radiative transition takes place between E_3 and E_2 with a photon energy $\hbar\omega \approx 30$ meV. Electrons then quickly depopulate from E_2 to E_1 because E_2-$E_1 > \hbar\omega_{LO}$. The spontaneous emission efficiency of this four-level system is given by:

$$\eta_{4L} = \sigma_{41} n_1 \frac{\omega_{32}}{\omega_{41}} \frac{\tau_4^{tot}}{\tau_{43}} \frac{\tau_3^{tot}}{\tau_{32}^{rad}}. \tag{5}$$

At first sight it looks like this result is worse than the three-level case because of the additional factor τ_4^{tot}/τ_{43}. Actually it is this extra ratio that allows us to bypass a major deficiency of the three-level design. We can now design the scattering rates such that $1/\tau_{43}$ is the dominant contribution to $1/\tau_4^{tot}$ so that $\tau_4^{tot}/\tau_{43} \sim 1$. Thus the absorption of the pump $\sigma_{41}n_1$ is now effectively decoupled from the LO-phonon scattering $1/\tau_3^{tot}$. We can increase the dipole moment z_{41} to increase σ_{41} without affecting $1/\tau_3^{tot}$. This gives us the extra flexibility to increase the emission efficiency over the simpler three-level design.

Fig. 18(a) shows a calculation of the emission efficiency as a function of electron density n_1 for both the three-level and the four-level structures. Clearly, the four-level scheme gives an order of magnitude improvement at the electron density of $2.5\times10^{11}/cm^2$. The maximum efficiency for the four-level structure occurs when E_4-$E_3 \approx \hbar\omega_{LO}$, at which the rate $1/\tau_{43}$ is the highest.

The same physics that allows us to improve the spontaneous emission efficiency also leads to a larger population inversion and therefore gain. Fig. 18(b) shows the calculated

gain for 1 W of pump power and a 6-meV linewidth. The active region is composed of 100 modules of the three-well structures separated by 200-Å barriers. It is apparent that the gain of the four-level design scheme is an order of magnitude greater than the three-level design at moderate electron densities.

Extending this design analysis one step further, we have also analyzed a five-level structure, with the lower radiative level separated from the level below by $\sim\hbar\omega_{LO}$. Because of the enhanced depopulation rate at this resonance, the population on the lower radiative level can be kept low even with a fast relaxation from the upper radiative level. This feature is attractive as it is important for high-temperature operations. At elevated temperatures, the LO-phonon scattering of hot electrons significantly increases the relaxation scattering between the two radiative subband levels.[21]

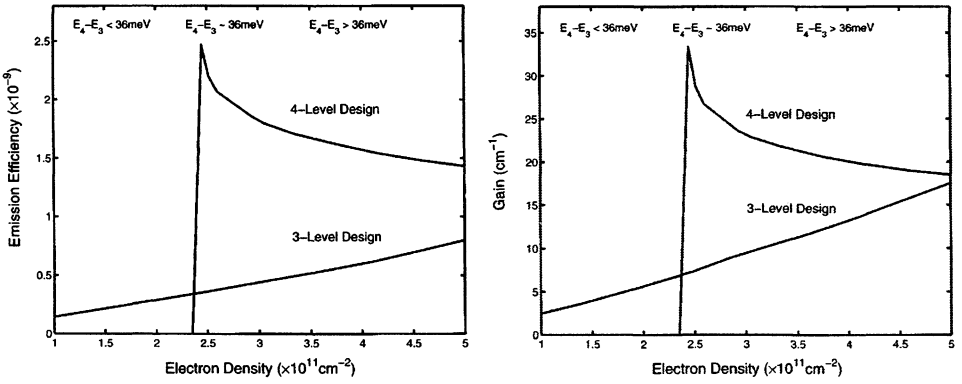

Figure 18. (a) Comparison of emission efficiency for the three-level and four-level designs. (b) Comparison of gain for the three-level and four-level design.

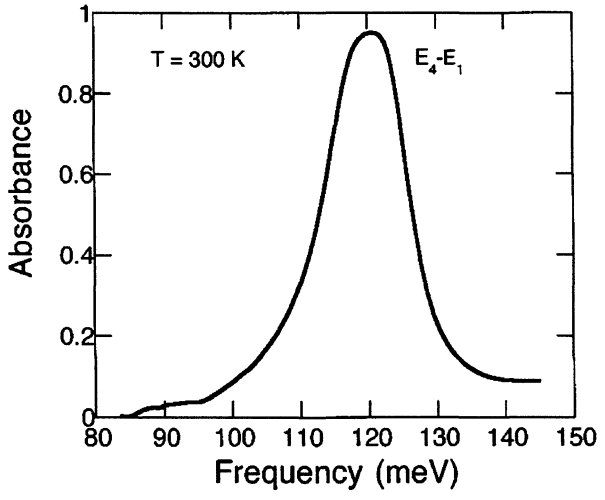

Figure 19. Mid-infrared transmission measurement of the four-level quantum-well structure. The measured E_4-E_1 peak position is at 119.8 meV with a FWHM of 13.4 meV.

We have grown a four-level structure whose band diagram is shown in Fig. 17(b). Fig. 19 shows the absorption spectrum of the device. The absorbance is obtained by taking the ratio of the transmitted beam with its electrical field in the plane of the quantum wells and perpendicular to the plane. The main peak at 120 meV in the absorption spectrum is due to the 1→4 intersubband transition, which occurs at the designed photon energy of 119.5 meV (corresponding to $\lambda \approx 10$ μm).

The THz emission measurements were carried out using the set-up shown in Fig. 20. In this set-up, the input CO_2 laser beam and the output THz beam are at orthogonal angle so that the output is not contaminated by the strong CO_2 laser beam. The measurements are more difficult than those of electrically pumped THz emitters, because both the input and output need to be well aligned and the output power levels are weaker than those from the electrically pumped emitters. Nonetheless, we have obtained emission spectra that showed strong evidence of THz emission due to intersubband transitions.

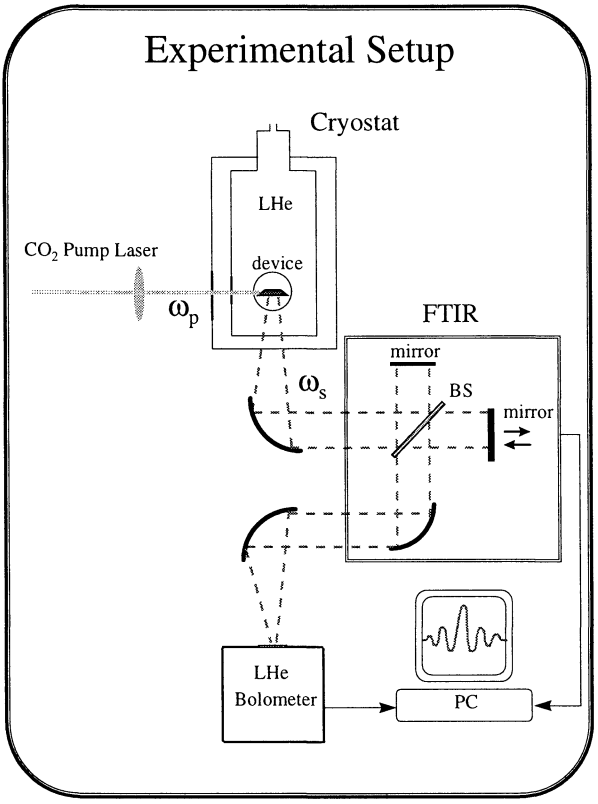

Figure 20. Emission measurement set-up for the optically pumped intersubband THz emitters.

Fig. 21 shows representative emission spectra. The solid curve corresponds to the pump being tuned to resonance, while the dashed line is the spectrum when the pump is tuned off resonance. At off resonance, only bulk absorption can take place and the

emission mainly results from blackbody radiation. Thus the dashed curve in Fig. 21 provides an estimate on the background of thermal radiation. In the solid curve, there is a prominent peak centered at ~31 meV, which is close to the designed value of 3→2 transition. A Lorentzian curve fit gives a FWHM of ~7 meV, which is a relatively narrow linewidth compared to the room-temperature linewidth of the absorption spectrum. As can be seen from Fig. 21, the 3→2 emission peak lies on top of a broad blackbody spectrum. The strong blackbody radiation is a result of low emission efficiency of the (intersubband) optically pumped THz emitters.

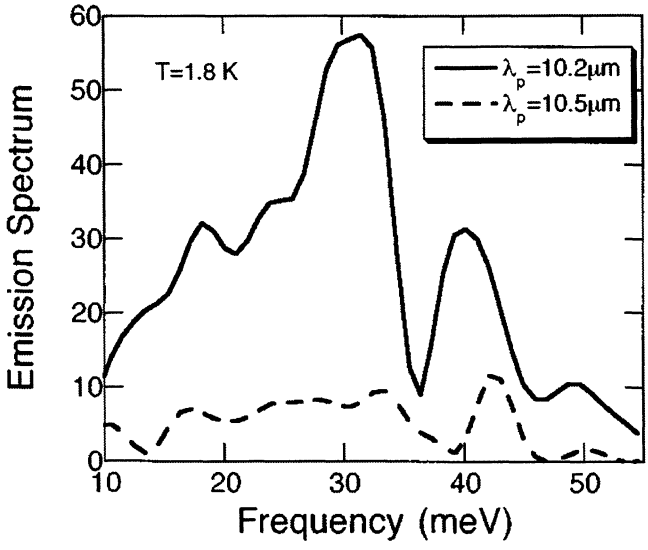

Figure 21. THz emission spectra. 0.2-W of cw pump power was coupled into the sample. The solid curve corresponds to when the pump frequency is tuned to the 1→4 transition resonance, while the dashed curve corresponds to the case of off resonance. The main emission peak of the solid curve is at 30.8 meV with a FWHM of 7 meV.

3.3 Interband optically pumped THz emitters

Our investigation discussed in section 3.2 showed some interesting results, namely that we can explore subband engineering to improve THz emission efficiency and gain. However, it also showed the drawbacks of (intersubband) optically pumped THz emitters. The much stronger blackbody radiation shown in Fig. 21 compared to the electrically pumped THz emitters shown in Figs. 5 and 11 indicates that the emission efficiency of the optically pumped emitters is much lower than their electrically pumped counterparts. The main reason of this low emission efficiency is the inseparable coupling between the pumping and the relaxation processes. In order to have a large pump cross section, the ground-state level and the top level must have a strong spatial overlap, which will result in a very fast relaxation due to electron-LO-phonon scattering.

It was to overcome this challenge that motivated us to explore the feasibility of interband optically pumped THz lasers.[22] The core of these structures is a three-well

module, as shown in Fig. 22. In these structures, the pump process (which is due to interband excitations) and the relaxation process (which is mostly due to intersubband scatterings) are largely decoupled. Consequently, a relatively long lifetime of the upper subband level can be engineered along with a high pump efficiency. The less favorable Manley-Rowe relation of the interband pumping compared to that of the intersubband pumping will not result in additional heating, as a large portion of the pump photon energy will be removed from the devices via interband lasing at a slightly lower photon energy. The absence of doping will likely yield narrower emission linewidths and lower cavity losses. Furthermore, the absence of a selection rule in the interband pumping scheme allows a convenient surface pumping without using diffractive gratings.

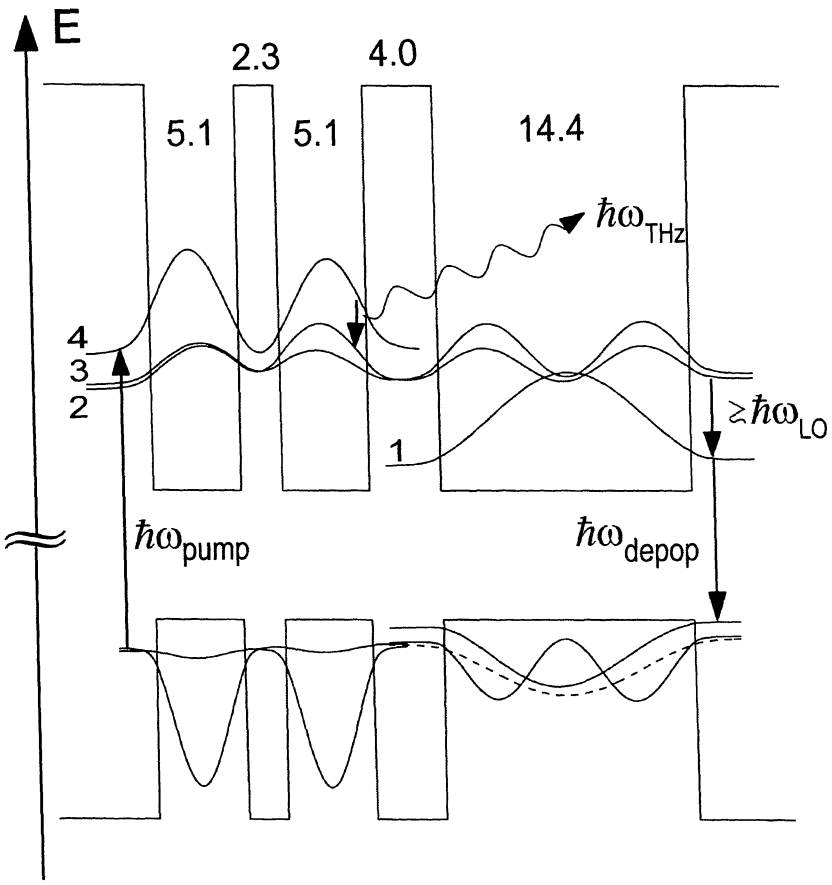

Figure 22. Computed conduction and valence band profiles and squared magnitude wave functions for the interband optically pumped THz emitters. Layer thicknesses in nm are displayed above the layers. In the valence band, heavy-hole subbands are indicated with solid lines, light-hole subbands with dashed lines.

As far as the intersubband transitions in the conduction band are concerned, the structure is essentially a four-level system c_1-c_4, with the top two conduction subbands

forming the radiative pair for THz emission. Electrons are optically pumped to c_4, which acts as the upper level for a radiative transition into c_3. The lower level c_3 is strongly coupled to the first excited level c_2 in the wide well. These two levels are at anticrossing and form a doublet with a strong spatial overlap. The calculated energy separation E_{43} is 18.6 meV (corresponding to ~4.6 THz) with a dipole moment $z_{43} \approx 36$ Å, and $E_{32} \approx 3$ meV. In order to obtain a fast depopulation of the c_3/c_2 doublet, the energy separation E_{21} is designed to be slightly greater than $\hbar\omega_{LO}$. Scattering down from the higher-energy subbands, electrons will pile up in c_1 until the interband lasing threshold is reached for the transition between c_1 and the highest valence subband.

We used a two-band **k•p** model to calculate the valence subband levels and wave functions,[23,24] and from which we can compute the interband radiative transition strengths. The intersubband relaxation processes in the conduction band were calculated self-consistently including both electron-LO-phonon scattering and electron-electron scattering. The rates of electron-electron scattering were calculated using a numerical Hartree code.[25] The main results are presented in Fig. 23. In Fig. 23(a), the electron-LO-phonon scattering times of several processes are plotted as functions of electron temperature. As can be seen from the figure, the 2→1 and 3→1 always have the shortest times because the wave functions of the involved subbands have strong spatial overlaps. Fig. 23(b) shows the populations of the four conduction subbands vs. the electron temperature. It appears that a population inversion ($n_4 > n_3$) exists at temperatures as high as 70 K. Fig. (c) and (d) show the calculated emission efficiency and gain vs. the electron temperature. Note that even with an unfavorable Manley-Rowe relation, the calculated emission efficiency is approximately two orders of magnitude higher than that for an intersubband pumped emitter (see Fig. 18(a)). This is largely because the decoupling between the pumping and relaxation processes in the interband pumped scheme. The upper-level lifetime τ_4 can be made much longer than that in intersubband pumped schemes. Finally, the estimated value of gain is ~50 cm^{-1} at 50 K at a pumping level of 30 kW/cm^2, which should be achievable, at least in a pulsed mode.

In summary, we have investigated both electrically and optically pumped intersubband THz emitters with the goal to develop coherent THz laser sources. By far, the electrically pumped structures have shown much greater promise in terms of their radiation characteristics and our understanding of the transport processes in the devices. We strongly believe that with careful fine tuning as discuss in Section 2, THz lasing should be achieved in the near future. Needless to say, such a development will have a qualitative impact on the science and technology in the THz electromagnetic spectrum, which is currently severely underutilized mainly because of lack of coherent sources.

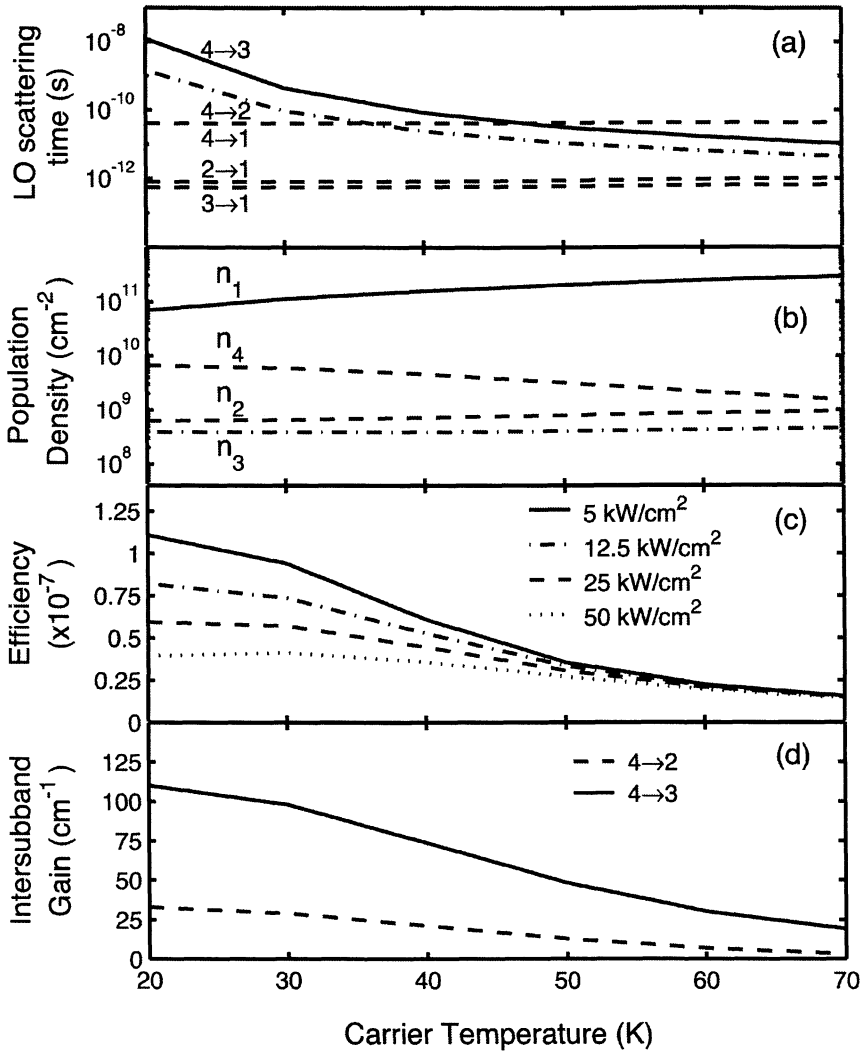

Figure 23. (a) Electron-LO-phonon scattering times and (b) subband populations versus temperature for a pump intensity of 30 kW/cm^2. In (c) the temperature dependence of the THz emission efficiency is displayed for several pump intensities. (d) Temperature dependence of the intersubband gain for a pump intensity of 30 kW/cm^2 and spontaneous emission linewidth of 2 meV.

Acknowledgments

The author would like to thank several of his current and former students, B. Xu, I. Lyubomirsky, B. S. Williams, H. Callebaut, and S. Kumar for their contributions during various stages of the project. He would also like to thank M. R. Melloch and J. L. Reno for providing high-quality MBE wafers for the project. This work has been supported by AFOSR, NASA, NSF, and ARO.

References

1. R. F. Kazarinov and R. A. Suris, "Possibility of amplification of electromagnetic waves in a semiconductor with a superlattice," *Sov. Phys. Semicond.* **5**, (1971) 707--709.
2. J. Faist, F. Capasso, D. L. Sivco, C. Sirtori, A. L. Hutchinson, and A. Y. Cho, "Quantum cascade laser," *Science* **264**, (1994) p. 477.
3. R. Colombelli *et al*, "Far-infrared surface-plasmon quantum-cascade lasers at 21.5 and 24 μm wavelengths," *Appl. Phys. Lett.* **78**, (2001) 2620--2622.
4. M. Rochat, M. Beck, J. Faist, and U. Oesterle, "Measurement of far-infrared waveguide loss using a multisection single-pass technique," *Appl. Phys. Lett.* **78**, (2001) 1967--1969.
5. M. Rochat, J. Faist, M. Beck, U. Oesterle, and M. Ilegems, "Far-infrared ($\lambda = 88$ μm) electroluminescence in a quantum cascade structure," *Appl. Phys. Lett.* **73**, (1998) 3724--3726.
6. B. S. Williams, H. Callebaut, Q. Hu, and J. Reno, "Magnetotunneling spectroscopy of resonant anticrossing in terahertz intersubband emitters," *Appl. Phys. Lett.* **79**, (2001) 4444--4446.
7. B. Xu, Q. Hu, and M. R. Melloch, "Electrically pumped tunable THz emitters based on intersubband transition," *Appl. Phys. Lett.* **71**, (1997) 440--442.
8. B. S. Williams, B. Xu, Q. Hu, and M. R. Melloch, "Narrow-linewidth terahertz intersubband emission from three-level systems," *Appl. Phys. Lett.* **75**, (1999) 2927--2929.
9. M. Dutta and M. A. Stroscio, "Comment on 'Energy level schemes for far-infrared quantum well lasers'," *Appl. Phys. Lett.* **74**, (1999) p. 2555; Q. Hu and I. Lyubomirsky, *Appl. Phys. Lett.* **74**, (1999) p. 3065.
10. B. S. Williams and Q. Hu, "Optimized energy separation for phonon scattering in three-level terahertz intersubband lasers," *J. Appl. Phys.* **90**, (2001) 5504--5511.
11. S. G. Yu, K. W. Kim, M. A. Stroscio, G. J. Iafrate, J. -P. Sun, and G. I. Haddad, "Transfer matrix method for interface optical-phonon modes in multiple-interface heterostructure systems," *J. Appl. Phys.* **82**, (1997) 3363--3367.
12. H. C. Liu *et al.* Appl. Phys. Lett. **78**, (2001) 3580--3582.
13. J. H. Smet, C. G. Fonstad, and Q. Hu, "Magneto-tunneling spectroscopy in Wide InGaAs/InAlAs Double Quantum Wells," *Appl. Phys. Lett.* **63**, (1993) 2225--2227.
14. J. Ulrich, R. Zobl, W. Schrenk, G. Strasser, K. Unterrainer, and E. Gornik, "Terahertz quantum cascade structures: Intra- versus interwell transition," *Appl. Phys. Lett.* **77**, (2000) 1928--1930.
15. R. Köhler, R. C. Iotti, A. Tredicucci, and F. Rossi, "Design and simulation of terahertz quantum cascade lasers," Appl. Phys. Lett. **79**, (2001) 3920--3922.
16. C. Sirtori, F. Capasso, J. Faist, L. N. Pfeiffer, and K. W. West, "Far-infrared generation by doubly resonant difference frequency mixing in a coupled quantum well two-dimensional electron gas system," Appl. Phys. Lett. **65**, (1994) 445--447.
17. E. Rosencher and Ph. Bois, "Model system for optical nonlinearity: asymmetric quantum wells," Phys. Rev. **B44**, (1991) p. 11315.
18. I. Lyubomirsky and Q. Hu, "Optical parametric oscillators without phase matching," J. Opt. Soc. Am. **B14**, (1997) 984--988.

19. I. Lyubomirsky and Q. Hu, "Energy level schemes for far-infrared quantum well lasers," *Appl. Phys. Lett.* **73**, (1998) 300--302.
20. I. Lyubomirsky, Q. Hu, and M. R. Melloch, "Measurement of far-infrared intersubband spontaneous emission from optically pumped quantum wells," *Appl. Phys. Lett.* **73**, (1998) 3043--3045.
21. I. Lyubomirsky, Ph. D. thesis, "Toward Far-infrared Quantum Well Lasers," MIT (1999) (unpublished).
22. H. Callebaut, Master's thesis, "GaAs/AlGaAs Far-infrared Quantum Well Lasers," MIT (2001) (unpublished).
23. J. M. Luttinger and W. Kohn, "Motion of electrons and holes in perturbed periodic fields," Phys. Rev. **97**, (1955) 869--883.
24. D. A. Broido and L. J. Sham, "Effective masses of holes at GaAs/AlGaAs heterojunctions," Phys. Rev. **B31**, (1985) 888-892.
25. The code used in our calculations of electron-electron scattering is from P. Harrison, "Quantum wells, wires, and dots," John Wiley and Sons, Chichester, UK, (1999).